Kramers Rate Theory of Pacemaker Dynamics in Noisy Excitable Media

Zhaoyang Zhang,[1] Gang Hu,[2] Yuhao Zhang,[1] and Zhilin Qu[3,*]

[1]*Department of Physics, School of Physical Science and Technology, Ningbo University, Ningbo, Zhejiang 315211, China*
[2]*Department of Physics, Beijing Normal University, Beijing 100875, China*
[3]*Department of Medicine, University of California, Los Angeles, California 90095, USA*

Rhythmic activities, which are usually driven by pacemakers, are common in biological systems. In noisy excitable media, pacemakers are self-organized firing clusters, but the underlying dynamics remains to be elucidated. Here we develop a Kramers rate theory of coupled cells to describe the firing properties of pacemakers and their dependence on coupling strength and system size and dimension. The theory captures accurately the simulation results of tissue models with stochastic Hodgkin-Huxley equations except when transitions from pacemakers to spiral waves occur under weak coupling.

Rhythmic activities are common in biological organisms [1–7], including heart rhythms, breathing, brain activities, circadian rhythm, cell or muscle contraction, and signaling in slime mold, etc. In most cases [8–11], the rhythmic signal originates from a site, called a pacemaker, and then conducts throughout the whole system to execute biological functions. In general, a pacemaker is assumed as a group of cells that exhibit limit cycle oscillations. However, instead of limit cycle oscillators, pacemakers may form via tissue-scale dynamical instability [12] or self-organized random firing clusters in noisy excitable media [10,11]. Under normal healthy conditions, some of the rhythms are highly periodic, such as the circadian rhythm, but some exhibit large variabilities, such as heart rhythms, brain activities, or calcium oscillations [4,13–17]. Changes of the rhythm properties may imply diseases, such as increased risk of sudden cardiac death [13] or seizures [2,3,16]. Therefore, understanding the dynamics of pacemakers is of great importance for understanding normal biological rhythms and disease development.

In excitable cells, noise can cause a quiescent cell to fire stochastically [18–21]. When these cells are coupled to form a tissue, pacemakers are self-organized, occurring randomly in both space and time [10,11,21–25]. Although the firing dynamics in noisy excitable media have been widely investigated in computer simulations, a rigorous theory has not been established. In this study, we develop a Kramers rate theory that accounts for the firing dynamics in tissue (coupled cells) and their dependence on coupling strength, tissue size, and dimension. The theory captures accurately the simulation results of tissue models with stochastic Hodgkin-Huxley (HH) equations.

Simulations are carried out in single cell, one-dimensional (1D) cable and two-dimensional (2D) tissue with the following partial differential equation for voltage (V):

$$\frac{\partial V}{\partial t} = -\frac{I_{\text{ion}}}{C_m} + D\nabla^2 V, \qquad (1)$$

where I_{ion} is the total current density, $C_m = 1~\mu\text{F/cm}^2$ is the membrane capacitance, and D is the diffusive coupling constant. I_{ion} is from the HH model [26] with noise incorporated into the gating variables using the formulism by Fox [27]. We use ε to describe the noise strength. Model details are in Supplemental Material [28].

For the original HH model, it remains quiescent unless a suprathreshold stimulus is given. In the presence of noise, stochastic firings occur [Fig. 1(a), and see also a recording in a shorter time window in Fig. S1(a) [28]], and the firing intervals (T) exhibit an exponential distribution except for short intervals. The averaged firing interval ($\bar{T}$) and standard deviation (σ) increase exponentially with the inverse of noise strength ($1/\varepsilon$), and $\sigma = \bar{T}$ unless when the noise is strong ($1/\varepsilon$ is small). Recordings from 1D cable [Fig. 1(b)] and 2D tissue [Fig. 1(c)] exhibit the same features, except that $\bar{T}$ becomes longer in one and two dimensions. Figure 1(d) is a space-time plot of V from a 1D cable, and Fig. 1(e) plots V snapshots from a 2D tissue, showing randomly occurring pacemakers. For all cases, if we plot σ versus $\bar{T}$, it obeys $\sigma = (\bar{T} - T_{\min})$ (see Fig. S1(b) [28]), with $T_{\min}$ accounting for refractoriness. This type of relationship was observed for calcium spikes in real cells and simulations [4,17,29].

The dependences of $\bar{T}$ on coupling strength (D), system size (N), and dimension are shown in Fig. 2. Figures 2(a) and 2(b) plot $\bar{T}$ versus D for different N for 1D cable [Fig. 2(a)] and 2D tissue [Fig. 2(b)]. $\bar{T}$ increases and then saturates as D increases except for very small D [see Fig. 4(a)]. For small D, $\bar{T}$ decreases with N [left panel in Fig. 2(c)], exhibiting an inverse relationship. As D becomes larger [middle and right panels in Fig. 2(c)], $\bar{T}$ first increases and then decreases with N. Furthermore, for
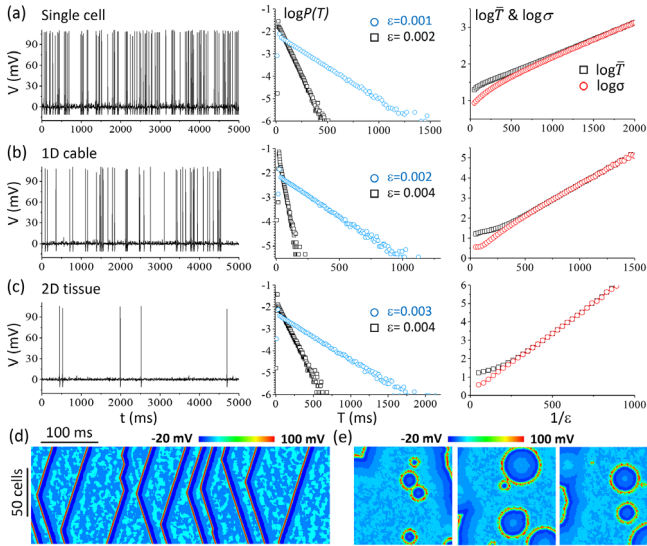
FIG. 1. Noise-induced firing properties and pacemakers in the HH model. (a) A single cell. (b) A 10-cell 1D cable. (c) A 3×3-cell 2D tissue. Left panels: V versus t recorded from a cell. The noise strength is $\varepsilon = 0.002$. Middle panels: $\log P(T)$ versus T for two noise strengths as marked. Right panels: $\log \bar{T}$ (black) and $\log \sigma$ (red) versus $1/\varepsilon$. (d) Time-space plot of voltage from a 100-cell 1D cable. (e) 3 voltage snapshots showing target patterns from a 100×100-cell 2D tissue. The diffusion constant is $D = 2 \times 10^{-4}$ cm^2/ms for (b) to (d) and $D = 9 \times 10^{-5}$ cm^2/ms for (e).

very large D, the increment of $\log \bar{T}$ ($\Delta \log \bar{T}$) as N increases to $N+1$ is a constant in 1D cable [Fig. 2(a)], independent of N. In 2D tissue [Fig. 2(b)], $\bar{T}$ increases more steeply and saturates earlier as D increases, and $\Delta \log \bar{T} \propto N$ roughly for very large D.
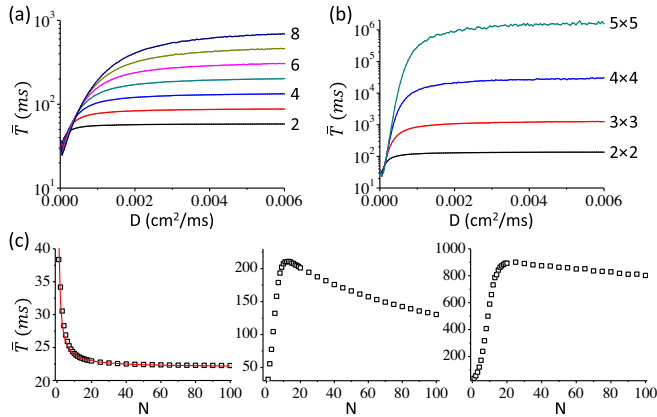

FIG. 2. Dependence of $\bar{T}$ on D and N in the HH model. (a) $\bar{T}$ versus D from 1D cables of different sizes. (b) $\bar{T}$ versus D from 2D tissue of different sizes. (c) $\bar{T}$ versus N for 1D cables for $D = 0.00005$ (left), $D = 0.001$ (middle), and $D = 0.002$ (right) cm^2/ms. The red curve in the left panel is $\bar{T} = 22 + 20/N$, in which the 22 ms base is due to the recovery of the HH model (see Fig. S1 [28]). $\varepsilon = 0.0035$ for (a) to (c).

The results in Fig. 1 imply that the firing dynamics in tissue may still follow the Kramers rate theory. Since the firing in the HH model is a threshold phenomenon, to facilitate theoretical analysis, we use the simplest prototype model for Kramers escape process and couple them together to investigate the pacemaker dynamics. The simplest model describing the Kramers escape process is

$$\frac{dx}{dt} = x(x - a) + \sqrt{2\varepsilon}\xi(t), \quad (2)$$

where $\xi(t)$ is a Gaussian white noise satisfying $\overline{\xi(t)} = 0$ and $\overline{\xi(t)\xi(t')} = \delta(t - t')$. $x = 0$ is the potential well and $x = a$ is the potential barrier. The transition rate (γ) is [30,31]

$$\gamma = \frac{1}{2\pi}\sqrt{U_0''|U_a''|}e^{(U_0 - U_a)/\varepsilon} = \frac{a}{2\pi}e^{-a^3/6\varepsilon}, \quad (3)$$

where U is the potential, i.e., $U(x) = -\frac{1}{3}x^3 + (a/2)x^2$, and U_0 is U at $x = 0$ and U_a is U at $x = a$. The distribution of the first-passage time or firing interval (T) is

$$P(T) = \gamma e^{-\gamma T}. \quad (4)$$

The average firing interval $\bar{T}$ and standard deviation σ are

$$\bar{T} = \sigma = \frac{1}{\gamma} = \frac{2\pi}{a}e^{a^3/6\varepsilon}. \quad (5)$$

The simulation results of the single cell [Fig. 1(a)] agree well with the general Kramers theory. Now we consider a 1D cable of N cells with nearest-neighbor coupling, i.e.,

$$\frac{dx_n}{dt} = x_n(x_n - a) + D(x_{n-1} + x_{n+1} - 2x_n) + \sqrt{2\varepsilon}\xi_n(t), \quad (6)$$

where $n \in [1, N]$. In a recent study, Falcke and Friedhoff [32] derived analytically the first-passage time and its dependence on system size in a linear Markovian chain of states using the master equation. Here we derive the first-passage time or transition rate for 1D [Eq. (6)] and 2D [Eq. (S20) [28]] prototype models following the Kramers theory.

The corresponding Fokker-Planck equation of Eq. (6) is

$$\frac{\partial P}{\partial t} = -\sum_{n=1}^{N}\left[\frac{\partial}{\partial x_n}f(x_n)P + \varepsilon\frac{\partial^2 P}{\partial x_n^2}\right], \quad (7)$$

where $P = P(x_1, x_2, \ldots, x_n, \ldots, x_N, t)$ and $f(x_n) = x_n(x_n - a) + D(x_{n-1} + x_{n+1} - 2x_n)$. The steady-state solution of Eq. (7) can be expressed as $P(x_1, x_2, \ldots, x_n, \ldots, x_N) \propto e^{-U(x_1, x_2, \ldots, x_n, \ldots, x_N)/\varepsilon}$ with U explicitly expressed as,
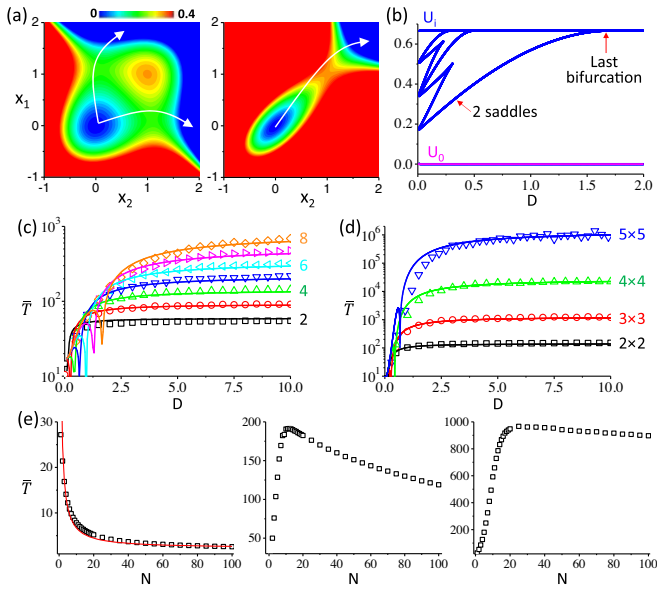
FIG. 3. A Kramers theory based on the prototype model. (a) Color maps of U for a two-cell system for $D = 0.2$ (left) and $D = 2$ (right). (b) U_0 and U_i versus D for a 4-cell cable. $a = 1$. (c) $\bar{T}$ versus D from 1D cables with different sizes. Symbols are simulation results of Eq. (6) and lines are theoretical results. (d) $\bar{T}$ versus D from simulations (symbols) and theory (lines) of 2D tissue with different sizes. The theoretical results are calculated using 4 saddles of the lowest U_i before the bifurcation. (e) $\bar{T}$ versus N for $D = 0.11$ (left), 2.2 (middle), and 4.4 (right). The red line in the left panel is $\bar{T} = 2.2 + 45/N$. $a = 0.255$ and $\varepsilon = 0.0063$ for (c) to (e), which are the same as the ones used for the theory in Fig. S4 [28]. The results in (c) to (e) match quantitatively with those in Fig. 2.

$$U = -\sum_{n=1}^{N}\left[\frac{1}{3}x_n^3 - \frac{a+2D}{2}x_n^2 + \frac{D}{2}(x_{n-1}+x_{n+1})x_n\right]. \quad (8)$$

Applying $\partial U/\partial x_n = 0$, one obtains a set of algebra equations for fixed-point solutions, which are identical to those by setting $dx_n/dt = 0$ in Eq. (6) without the noise term. Figure 3(a) plots the U landscapes for a 2-cell system for a small D (left) and a large D (right). When D is small, there are 4 solutions: a stable node, an unstable node, and two saddles. As D increases, the two saddles and the unstable node collapse into a single saddle (Fig. S2 [28] plots more panels of landscapes of U to show this process). Figure 3(b) shows U at the fixed-point solutions (labeled as U_0 and U_i) versus D for a 4-cell system [Fig. S2(b) [28] shows U_i and associated number of fixed-point solutions for 3 system sizes]. In general, the number of solutions is between 2 and 2^N. There are one stable node ($x_1 = x_2 = \ldots = x_N = 0$) and one unstable node ($x_1 = x_2 = \ldots = x_N = a$), and the rest are saddles. As D increases, the system undergoes multiple bifurcations in which a pair of saddles collapses with each other or into the unstable node (see Fig. S3 [28] for an example

of this process in a 4-cell system). After the last bifurcation, the system has only one stable node and one saddle.

The system can escape the stable node via any of the saddles [e.g., Fig. 3(a)]. We assume that the escape paths are independent, then the probability that the system stays inside the potential well is described by

$$\frac{dp}{dt} = -\gamma p = -\sum_{i=1}^{M}\gamma_i p, \quad (9)$$

where M is the total number of saddles, $\gamma = \sum_{i=1}^{M}\gamma_i$ is the total transition rate. γ_i is the transition rate across the ith saddle, which is calculated as [30,31]

$$\gamma_i = \frac{1}{2\pi}\sqrt{\left|\lambda_1^0\lambda_1^i\prod_{n=2}^{N}\frac{\lambda_n^0}{\lambda_n^i}\right|}e^{(U_0-U_i)/\varepsilon}, \quad (10)$$

where λ_n^0 are the eigenvalues of the stable node and λ_n^i are the eigenvalues of the ith saddle. In general, one needs to obtain the fixed-point solutions and their eigenvalues numerically to calculate γ_i. However, one can solve the problem analytically for a 2-cell system and for many cells under certain conditions. For a 2-cell system, the bifurcation occurs at $D_c = a/2$ at which the two saddles coalesce with the unstable node. When $D < a/2$ (see Supplemental Material [28]), $\gamma = (1/\pi)\sqrt{|a[D+\sqrt{D^2+(a+2D)(a-2D)}]^2/(a-2D)|}$ $e^{-(a+2D)^2(a-D)/6\varepsilon}$. When $D \to 0$, $\gamma \to (a/\pi)e^{-a^3/6\varepsilon}$, which is twice the rate of the single cell [Eq. (3)]. As D increases, γ decreases (dominated by the exponential component), but as D is close to $a/2$, the square root term dominates, causing γ to approach infinity. When $D > a/2$, $\gamma = (a/2\pi)\sqrt{|(a+2D)/(a-2D)|}e^{-a^3/3\varepsilon}$.

Although explicit expressions of γ cannot be obtained for systems larger than 2 cells, they can be obtained under certain limits, such as small D and large D. At $D = 0$, the fixed-point solutions are simply the combinations of those of the N uncoupled cells, and thus there are 2^N solutions. Since $U = 0$ ($x = 0$) and $U = a^3/6$ ($x = a$) for a single cell, then U for the whole system is $U_0 = 0$ and $U_i = na^3/6$ ($n = 1, 2, \ldots, N$) with C_N^n solutions in group n. U_i bifurcates as D increases [Fig. 3(b) and Fig. S2(b) [28]]. Therefore, for $D \to 0$, we can approximate γ as

$$\gamma = \frac{a}{2\pi}\sum_{n=1}^{N-1}C_N^n e^{-na^3/6\varepsilon}. \quad (11)$$

Since γ_i decays exponentially with U_i, the major contributions are from the N saddles with the lowest U_i ($U_i = a^3/6$), and others can be ignored. Therefore, in the leading order, $\gamma \cong (Na/2\pi)e^{-a^3/6\varepsilon}$. This implies that $\bar{T}$

decreases inversely with N for small D, which is exactly the case in both the HH model [Fig. 2(c)] and the prototype model [Fig. 3(e)]. Similarly, for 2D and 3D tissue, at $D \to 0$, $\gamma \cong (N^2 a/2\pi)e^{-a^3/6\varepsilon}$ and $\gamma \cong (N^3 a/2\pi)e^{-a^3/6\varepsilon}$, respectively.

In 1D cable, when $D \geq D_c = a/2[1 - \cos(\pi/N)]$, the system has only one saddle and γ is then calculated as (see Supplemental Material [28]):

$$\gamma = \frac{a}{2\pi}\sqrt{\prod_{k=1}^{N-1}\left|\frac{a + 2D(1 - \cos\frac{k\pi}{N})}{a - 2D(1 - \cos\frac{k\pi}{N})}\right|}e^{-Na^3/6\varepsilon}. \quad (12)$$

When $D \to \infty$, $\gamma \to (a/2\pi)e^{-Na^3/6\varepsilon}$, and thus $\ln \bar{T} = (Na^3/6\varepsilon) + \ln(2\pi/a)$. This indicates that at large D, the increment of $\ln \bar{T}$, i.e., $\Delta \ln \bar{T} = (a^3/6\varepsilon)$, is independent of N. This agrees with the simulation results in Figs. 2(a) and 3(c). Transition rates similar to Eq. (12) can be obtained for 2D and 3D tissue (see Eqs. (S26) and (S27) [28]). When $D \to \infty$, $\gamma \to (a/2\pi)e^{-N^2 a^3/6\varepsilon}$ for 2D tissue and $\gamma \to (a/2\pi)e^{-N^3 a^3/6\varepsilon}$ for 3D tissue, which implies that $\ln \bar{T} = (N^2 a^3/6\varepsilon) + \ln(2\pi/a)$ for 2D tissue and $\ln \bar{T} = (N^3 a^3/6\varepsilon) + \ln(2\pi/a)$ for 3D tissue. Therefore, for 2D tissue and large D, $\Delta \ln \bar{T} = (2N + 1)a^3/6\varepsilon$, depending on N, agreeing with the simulation results in Figs. 2(b) and 3(d).

For $D > D_c$, one uses Eq. (12) to calculate γ. However, for $D < D_c$, one needs to obtain numerically the solutions of the saddles and their eigenvalues, and then use Eq. (10) to calculate γ (see description in Supplemental Material [28]). For intermediate D ($0 \ll D < D_c$), we can use the two saddles (four for 2D) with the lowest U_i [see Fig. 3(b) or Fig. S2(b) [28]] to calculate γ since the contribution of the higher ones can be ignored. Figures 3(c) and 3(d) compare the theoretical results (lines) with the simulation results (symbols) of the prototype model for 1D cable and 2D tissue, respectively. A quantitative comparison of the theory with the simulation results of the HH model in Figs. 2(a) and 2(b) is shown in Fig. S4 [28]. We also compare the theory with simulations of both the prototype model (Fig. S5 [28]) and the HH model (Fig. S6 [28]) with lower excitabilities, which shift D_c to a larger value to allow a better comparison for $D < D_c$. These results show that the theory agrees very well with the simulations of both models except at the bifurcations, where $\bar{T} \to 0$ since one of λ_n^i becomes zero (thus $\gamma \to \infty$). This is a caveat of the theory [Eq. (10)]. In the comparison of the theory with the results of the HH model, a and ε for the theory are determined only using two data points of the simulation results at large D and D is rescaled using data of one 1D cable (see Supplemental Material [28]). Interestingly, the theory using these parameter values matches quantitatively well with the results of the HH model and the prototype model and is applicable to any N and dimension.

This indicates that the theory captures well the dynamics of pacemaker firings in coupled systems.

The theory can provide a mechanistic explanation for the nonmonotonic dependence of $\bar{T}$ on N based on Eqs. (11) and (12). Since $D_c = a/2[1 - \cos(\pi/N)]$ for the last bifurcation, increasing N moves the bifurcation point to a larger D. Therefore, for a fixed D, when N is small, the system is in the right side of the bifurcation point, γ is then determined by Eq. (12), and thus $\bar{T}$ increases with N. When N is larger than a critical number, the system shifts to the left side of the bifurcation point. According to Eq. (11), contributions from multiple saddles cause $\bar{T}$ to decrease with N. These two competing effects result in the nonmonotonic dependence of $\bar{T}$ on N.

A nonmonotonic dependence of $\bar{T}$ on D is also observed for weak coupling in both 1D and 2D models, i.e., $\bar{T}$ first decreases and then increases as D increases from zero [Fig. 4(a)]. This behavior was also reported previously [24,33,34]. Our theory provides a mechanistic interpretation for this behavior. Based on Eqs. (3) and (11), once $D > 0$, $\bar{T}$ will change suddenly from $\bar{T} = (2\pi/a)e^{a^3/6\varepsilon}$ for a single cell to $\bar{T} = (2\pi/Na)e^{a^3/6\varepsilon}$ for an N-cell cable or $\bar{T} = (2\pi/N^2 a)e^{a^3/6\varepsilon}$ for an $N \times N$-cell tissue. That is, as D increases from zero, $\bar{T}$ begins to decrease suddenly. However, the decrease is more gradual in the HH model due to the source-sink effect.

When the tissue size is large enough, phase transitions of the spatiotemporal dynamics occur under weak coupling. Figure 4(b) shows voltage snapshots for different D values in a 100×100 cell tissue. There are three phase transitions as marked by the arrows in Fig. 4(a). The first transition is
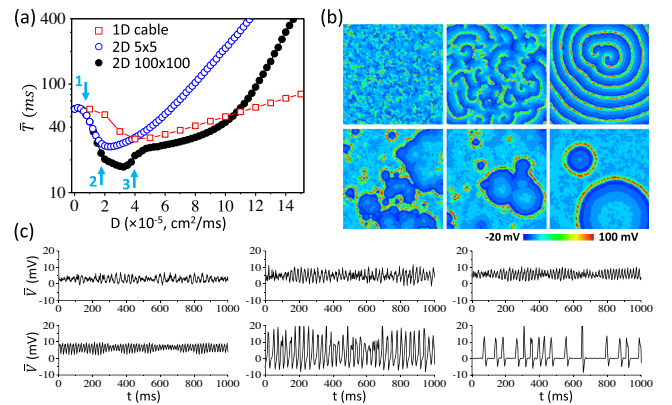

FIG. 4. Effects of weak coupling on $\bar{T}$ and spatiotemporal dynamics in the HH model. (a) $\bar{T}$ versus D for a 10-cell cable, 5×5-cell tissue, and 100×100-cell tissue. (b) Voltage snapshots for different D values in the 100×100 cell tissue. Top: from left to right $D = 1 \times 10^{-5}$, $D = 2 \times 10^{-5}$, and $D = 3 \times 10^{-5}$ cm^2/ms. Bottom: from left to right, $D = 4 \times 10^{-5}$, $D = 5 \times 10^{-5}$, and $D = 12 \times 10^{-5}$ cm^2/ms. (c) Averaged voltage from a 20×20-cell area in the center region for the same D values as in (b). $\varepsilon = 0.002$.

from uncoupled individual firings to collective firings. In this regime (D is very small), the system exhibits small firing clusters without propagation [top left in Fig. 4(b)]. As D increases, the pattern changes from firing clusters to glass-like patterns consisting of a mixture of spirals and firing clusters (top middle), and then to pure spiral waves (top right). As D increases further, the pattern changes from spiral waves to multiple foci or pacemakers (bottom panels). It is also unsurprising that the rhythm is more synchronous as D increases [Fig. 4(c)]. Similar transitions have been shown in experiments of cardiac excitable media [22,23].

Note that the occurring of spiral waves shortens $\bar{T}$ further [Fig. 4(a)]. This is because when spiral waves occur, the firing frequency is determined by the rotation of the spiral wave, and noise only has a small effect. In this region [between arrows 2 and 3 in Fig. 4(a)], the Kramers rate theory fails. As D increases, however, pacemakers occur, the Kramers rate theory remains valid, following the rules as shown in Figs. 2(b) and 3(d), as well as the same σ and $\bar{T}$ relationship, i.e., $\sigma = (\bar{T} - T_{\min})$ (see Fig. S7 [28]).

In conclusion, we develop a Kramers theory of coupled cells to describe the firing dynamics of pacemakers in noisy excitable media. The theory correctly describes the behaviors of the prototype model except at the bifurcation points. The prototype model (and the theory) captures well the behaviors of the HH model except when spiral waves occur at weak coupling. It provides mechanistic insights into the formation and dynamics of rhythmic activities in biological systems [1–11] as well as disease development. For example, the insight that as D increases, the firings occur via multiple barriers to via a single barrier, causing the firings to be more synchronous, agrees with that stronger gap junction coupling promotes seizure [35]. At weak coupling, transitions from pacemakers to spiral waves occur. This can account for sinus node tachycardia [36], or arrhythmogenesis in the atria and ventricles with fibrosis [37]. This can also be responsible for spontaneous spiral wave formation in the mammalian cortex [38,39] or slime mold [6,7].

———

*zqu@mednet.ucla.edu

[1] L. Glass, Synchronization and rhythmic processes in physiology, Nature (London) **410**, 277 (2001).

[2] P. J. Uhlhaas and W. Singer, Neural synchrony in brain disorders: Relevance for cognitive dysfunctions and pathophysiology, Neuron **52**, 155 (2006).

[3] P. Jiruska, M. de Curtis, J. G. R. Jefferys, C. A. Schevon, S. J. Schiff, and K. Schindler, Synchronization and desynchronization in epilepsy: Controversies and hypotheses, J. Physiol. **591**, 787 (2013).

[4] A. Skupin, H. Kettenmann, U. Winkler, M. Wartenberg, H. Sauer, S. C. Tovey, C. W. Taylor, and M. Falcke, How does intracellular Ca^{2+} oscillate: By chance or by the clock?, Biophys. J. **94**, 2404 (2008).

[5] I. R. Efimov, V. V. Fedorov, B. Joung, and S.-F. Lin, Mapping cardiac pacemaker circuits: Methodological puzzles of the sinoatrial node optical mapping, Circ. Res. **106**, 255 (2010).

[6] M. Falcke and H. Levine, Pattern Selection by Gene Expression in Dictyostelium Discoideum, Phys. Rev. Lett. **80**, 3875 (1998).

[7] K. J. Lee, E. C. Cox, and R. E. Goldstein, Competing Patterns of Signaling Activity in Dictyostelium Discoideum, Phys. Rev. Lett. **76**, 1174 (1996).

[8] G. Buzsáki, A. Smith, S. Berger, L. J. Fisher, F. H. Gage, G. Aston-Jones, and F. E. Bloom, Petit mal epilepsy and parkinsonian tremor: Hypothesis of a common pacemaker, Neuroscience (N.Y.) **36**, 1 (1990).

[9] M. H. Hastings, E. S. Maywood, and M. Brancaccio, Generation of circadian rhythms in the suprachiasmatic nucleus, Nat. Rev. Neurosci. **19**, 453 (2018).

[10] M. Falcke, On the role of stochastic channel behavior in intracellular Ca^{2+} dynamics, Biophys. J. **84**, 42 (2003).

[11] M. Nivala, C. Y. Ko, M. Nivala, J. N. Weiss, and Z. Qu, Criticality in intracellular calcium signaling in cardiac myocytes, Biophys. J. **102**, 2433 (2012).

[12] A. Yochelis, E. Knobloch, Y. Xie, Z. Qu, and A. Garfinkel, Generation of finite wave trains in excitable media, Europhys. Lett. **83**, 64005 (2008).

[13] A. L. Goldberger, L. A. N. Amaral, J. M. Hausdorff, P. C. Ivanov, C.-K. Peng, and H. E. Stanley, Fractal dynamics in physiology: Alterations with disease and aging, Proc. Natl. Acad. Sci. U.S.A. **99**, 2466 (2002).

[14] P. C. Ivanov, L. A. Amaral, A. L. Goldberger, S. Havlin, M. G. Rosenblum, Z. R. Struzik, and H. E. Stanley, Multifractality in human heartbeat dynamics, Nature (London) **399**, 461 (1999).

[15] Z. Qu, G. Hu, A. Garfinkel, and J. N. Weiss, Nonlinear and stochastic dynamics in the heart, Phys. Rep. **543**, 61 (2014).

[16] V. K. Jirsa, W. C. Stacey, P. P. Quilichini, A. I. Ivanov, and C. Bernard, On the nature of seizure dynamics, Brain **137**, 2210 (2014).

[17] K. Thurley, S. C. Tovey, G. Moenke, V. L. Prince, A. Meena, A. P. Thomas, A. Skupin, C. W. Taylor, and M. Falcke, Reliable encoding of stimulus intensities within random sequences of intracellular Ca^{2+} spikes, Sci. Signal. **7**, ra59 (2014).

[18] H. Qian, S. Saffarian, and E. L. Elson, Concentration fluctuations in a mesoscopic oscillating chemical reaction system, Proc. Natl. Acad. Sci. U.S.A. **99**, 10376 (2002).

[19] J. A. White, J. T. Rubinstein, and A. R. Kay, Channel noise in neurons, Trends Neurosci. **23,** 131 (2000).

[20] C. C. Chow and J. A. White, Spontaneous action potentials due to channel fluctuations, Biophys. J. **71,** 3013 (1996).

[21] B. Lindner, J. García-Ojalvo, A. Neiman, and L. Schimansky-Geier, Effects of noise in excitable systems, Phys. Rep. **392,** 321 (2004).

[22] G. Bub, A. Shrier, and L. Glass, Spiral Wave Generation in Heterogeneous Excitable Media, Phys. Rev. Lett. **88,** 058101 (2002).

[23] G. Bub, A. Shrier, and L. Glass, Global Organization of Dynamics in Oscillatory Heterogeneous Excitable Media, Phys. Rev. Lett. **94,** 028105 (2005).

[24] M. Nivala, C. Y. Ko, M. Nivala, J. N. Weiss, and Z. Qu, The emergence of subcellular pacemaker sites for calcium waves and oscillations, J. Physiol. **591,** 5305 (2013).

[25] P. Jung and G. Mayer-Kress, Spatiotemporal Stochastic Resonance in Excitable Media, Phys. Rev. Lett. **74,** 2130 (1995).

[26] A. L. Hodgkin and A. F. Huxley, A quantitative description of membrane current and its application to conduction and excitation in nerve, J. Physiol. **117,** 500 (1952).

[27] R. F. Fox, Stochastic versions of the Hodgkin-Huxley equations, Biophys. J. **72,** 2068 (1997).

[28] See Supplemental Material at http://link.aps.org/supplemental/10.1103/PhysRevLett.129.048101 for mathematical model, numerical methods, supplemental results and figures.

[29] A. Skupin and M. Falcke, From puffs to global Ca^{2+} signals: How molecular properties shape global signals, Chaos **19,** 037111 (2009).

[30] G. Hu, *Stochastic Forces and Nonlinear Systems* (Shanghai Scientific and Technological Education Publishing House, Shanghai, 1994).

[31] P. Hänggi, P. Talkner, and M. Borkovec, Reaction-rate theory: Fifty years after Kramers, Rev. Mod. Phys. **62,** 251 (1990).

[32] M. Falcke and V. N. Friedhoff, The stretch to stray on time: Resonant length of random walks in a transient, Chaos **28,** 053117 (2018).

[33] W. Y. Chiang, P. Y. Lai, and C. K. Chan, Frequency Enhancement in Coupled Noisy Excitable Elements, Phys. Rev. Lett. **106,** 254102 (2011).

[34] S. Liu, Z.-W. He, and M. Zhan, Firing rates of coupled noisy excitable elements, Front. Phys. **9,** 120 (2014).

[35] P. L. Carlen, F. Skinner, L. Zhang, C. Naus, M. Kushnir, and J. L. Perez Velazquez, The role of gap junctions in seizures, Brain Res. Rev. **32,** 235 (2000).

[36] J. A. Gomes, D. Mehta, and M. N. Langan, Sinus node reentrant tachycardia, PACE **18,** 1045 (1995).

[37] T. P. Nguyen, Z. Qu, and J. N. Weiss, Cardiac fibrosis and arrhythmogenesis: The road to repair is paved with perils, J. Mol. Cell. Cardiol. **70C,** 83 (2014).

[38] X. Huang, W. C. Troy, Q. Yang, H. Ma, C. R. Laing, S. J. Schiff, and J. Y. Wu, Spiral waves in disinhibited mammalian neocortex, J. Neurosci. **24,** 9897 (2004).

[39] S. J. Schiff, X. Huang, and J. Y. Wu, Dynamical Evolution of Spatiotemporal Patterns in Mammalian Middle Cortex, Phys. Rev. Lett. **98,** 178102 (2007).